

Using periodic orbits to compute chaotic transport rates between resonance zones

Sulimon Sattari^{1,2, a)} and Kevin A. Mitchell^{2, b)}

¹⁾*Research Institute for Electronic Science, Hokkaido University, Kita 20 Nishi 10, Kita-ku, Sapporo 001-0020, Japan*

²⁾*School of Natural Sciences, University of California, Merced, California, 95343*

(Dated: 29 July 2017)

Transport properties of chaotic systems are computable from data extracted from periodic orbits. Given a sufficient number of periodic orbits, the escape rate can be computed using the spectral determinant, a function that incorporates the eigenvalues and periods of periodic orbits. The escape rate computed from periodic orbits converges to the true value as more and more periodic orbits are included. Escape from a given region of phase space can be computed by considering only periodic orbits that lie within the region. An accurate symbolic dynamics along with a corresponding partitioning of phase space is useful for systematically obtaining all periodic orbits up to a given period, to ensure that no important periodic orbits are missing in the computation. Homotopic lobe dynamics (HLD) is an automated technique for computing accurate partitions and symbolic dynamics for maps using the topological forcing of intersections of stable and unstable manifolds of a few periodic anchor orbits. In this study, we apply the HLD technique to compute symbolic dynamics and periodic orbits, which are then used to find escape rates from different regions of phase space for the Hénon map. We focus on computing escape rates in parameter ranges spanning hyperbolic plateaus, which are parameter intervals where the dynamics is hyperbolic and the symbolic dynamics does not change. After the periodic orbits are computed for a single parameter value within a hyperbolic plateau, periodic orbit continuation is used to compute periodic orbits over an interval that spans the hyperbolic plateau. The escape rates computed from a few thousand periodic orbits agree with escape rates computed from Monte Carlo simulations requiring hundreds of billions of orbits.

Asteroid escape rates, chemical reaction rates, and fluid mixing rates are all examples of chaotic transport rates. One can compute transport rates by launching a Monte Carlo simulation over millions or billions of trajectories. However, it is possible to extract these rates from a much smaller number of specially selected trajectories. One method of doing so is by focusing on unstable periodic orbits, which form the skeleton for the behavior of chaotic dynamical systems. The local stretching near periodic orbits contributes to the overall escape rate, which can be computed from the spectral determinant, a function that incorporates the eigenvalues of the periodic orbits. We classify and find periodic orbits using finite-length segments of stable and unstable manifolds attached to certain key periodic orbits. In this way, the use of stable and unstable manifolds to compute periodic orbits can provide reliable estimates of chaotic transport rates in a broad range of deterministic chaotic dynamical systems.

I. INTRODUCTION

We study asymptotic transport rates in chaotic systems, namely the escape rates of trajectories from one region of phase space to another. The calculation of escape rates has direct physical applications such as computing atomic ionization rates, chemical reaction rates, and asteroid escape rates¹⁻⁵. Often, a chaotic system will exhibit an exponential decay at long times, given by

$$N(t) \rightarrow N_0 e^{-\gamma t}, \quad (1)$$

where $N(t)$ is the number of surviving trajectories as a function of time, N_0 is a constant, and γ is the asymptotic escape rate. The escape rate γ can be computed via Monte Carlo (MC) simulation by evolving an initial ensemble of points forward in time and counting the number of surviving trajectories as a function of time. Unfortunately a large number of initial points, often exceeding millions or billions, can be necessary to accurately resolve the asymptotic escape rate.

Our aim is to compute γ using fewer orbits, namely unstable periodic orbits. Gutzwiller^{6,7} made early insights into methods using periodic orbits when he developed the Gutzwiller trace formula, which he used to compute fluctuations in the quantum density of states for the anisotropic Kepler problem. (The computation of classical escape rates follows directly from Gutzwiller's semiclassical formulation.) Although Gutzwiller's original trace formula method did not permit the convergent computation of individual quantum eigenvalues, subsequent reformulations in terms of cycle expansions of spec-

^{a)}Electronic mail: sulimon@es.hokudai.ac.jp

^{b)}Electronic mail: kmitchell@ucmerced.edu

tral determinants, or “zeta functions,” provided better convergence properties. For example, Cvitanovic and Eckhardt⁸ successfully computed individual complex resonances of the three-disk scattering problem based on cycle expansions. An in-depth explanation of spectral determinants along with examples of quantum and classical escape-rate computations can be found in *The Chaos Book*⁹. More broadly, our work is also motivated by a large literature of theoretical and experimental work demonstrating the role of periodic orbits in quantum chaos^{10–16}.

For the three-disk scattering problem, the periodic orbits can be labeled by a simple symbolic itinerary based on the sequence of disks that are visited. In general, a system’s symbolic dynamics can be represented by a network. The nodes of the network correspond to regions in phase space, and the edges correspond to the allowed transitions between the regions. Once the system’s symbolic dynamics is constructed, one can write down the symbolic itinerary for any periodic orbit. This ability allows for accurately characterizing and computing all periodic orbits up to a chosen period, which is necessary to apply the spectral determinant and to compute escape rates. In many realistic physical systems, however, the construction of symbolic dynamics is not obvious, making the periodic orbits difficult to characterize and compute. *Our overarching goal is to compute escape rates in realistic physical systems from the spectral determinant by computing periodic orbits.* To achieve this goal, we will use recent methods in symbolic dynamics capable of representing general two-degree-of-freedom Hamiltonian systems. The ability to systematically compute symbolic dynamics and periodic orbits allows for applying periodic orbit theory to a broad range of physical applications, including studying the role of periodic orbits in quantum chaos in a real physical system, which is a future goal of this work.

One challenge we wish to address is computing escape rates in a mixed Hamiltonian phase space, where stable islands are embedded in a chaotic sea. The rich fractal structure of escape dynamics near the stable islands leads to two complications in computing the spectral determinant. The first complication is that the symbolic dynamics itself becomes very complex, requiring hundreds of symbols, and more complicated periodic orbits are necessary to converge to the true escape rate. The second complication is that mixed phase spaces tend to exhibit more pronounced multiexponential escape given by

$$N(t) \rightarrow N_0 e^{-\gamma_0 t} + N_1 e^{-\gamma_1 t} + N_2 e^{-\gamma_2 t} + \dots, \quad (2)$$

where N_0, N_1, N_2 are constants and $\gamma_0, \gamma_1, \gamma_2$ are different escape rates associated with different regions of phase space. An example of a bi-exponential escape rate is shown in Fig. 4. When the number of terms in Eq. (2) is infinite, one can obtain an algebraic escape curve.

We address these two complications by using a technique called homotopic lobe dynamics^{17,18} (HLD), which uses the topological forcing by intersections of stable and

unstable manifolds of a few anchor orbits to compute symbolic dynamics and partition the phase space. Using HLD, an arbitrarily accurate partition of phase space can be computed by incorporating longer and longer segments of the stable and unstable manifolds of anchor orbits. Moreover, the periodic orbits are identified by which region of phase space they occur in, and the distinct escape rates γ_i in Eq. (2) can be computed by using only periodic orbits that lie in the region of interest (see Sect. VII). The HLD technique can be used to specifically target the symbolic dynamics of a given region to search for periodic orbits in that region. The escape rate computed from the spectral determinant is compared to MC computations. For other approaches to symbolic dynamics of tangles, see Refs.^{19–29}.

Although we provide the machinery for computing the spectral determinant in a mixed phase space, we focus this study on a system where the accuracy of the symbolic dynamics can be verified. One way to verify the accuracy of symbolic dynamics is by checking the topological entropy, a measure of complexity and mixing in phase space. Once the symbolic dynamics is computed from HLD, the topological entropy is computed by taking the natural log of the largest eigenvalue of the transition matrix. Over the intervals of the Hénon map studied in Sect. VI, for example, the topological entropy computed from HLD matches the values computed using a method based on computational Conley index theory by Frongillo et. al.^{30,31}, and also matches the topological entropy values computed using pruning of symbolic dynamics by Hagiwara and Shudo³². Agreement in topological entropy indicates that our symbolic dynamics accounts for all periodic orbits. Therefore, by computing periodic orbits over hyperbolic plateaus, which are parameter intervals where the symbolic dynamics does not change, we can accurately compute the escape rate using the spectral determinant. We also study what happens to the convergence of the escape rate as the parameter is varied within and away from the hyperbolic plateau. To compute multiexponential escape rates, we focus on a parameter range where a subregion of phase space is within a hyperbolic plateau, while the full phase space has a higher topological entropy and may or may not be hyperbolic.

This paper is organized as follows. Section II summarizes the method for computing the escape rate from periodic orbits using the spectral determinant. Section III introduces the map used in our study, the area-preserving Hénon map. Section IV details the numerical technique for computing the escape rate directly from an MC simulation. Section V describes the full binary symbolic dynamics for a specific parameter interval of the Hénon map, and presents the escape rate data computed from periodic orbits over this parameter range. Section VI presents the symbolic dynamics for two hyperbolic plateaus of the Hénon map, along with periodic orbits and the escape rates computed from periodic orbits. Section VII presents the symbolic dynamics and escape

rates for a specific parameter range where the Hénon map exhibits multiexponential escape rates, namely a faster short-time escape rate and a slower, long-time escape rate. Section ?? compares the results computed from HLD with those computed from continuing orbits downward from the full shift on two symbols. Appendix A describes the details in extracting escape rate estimates from MC data by fitting an exponential function to the data. Appendix B describes the method of computing periodic orbits given a partition using HLD.

II. COMPUTING ESCAPE RATES FROM PERIODIC ORBITS USING THE SPECTRAL DETERMINANT

We present the derivation of a formula for spectral determinant for computing the escape rate γ in Eq. (1) following the discussion in Chaos Book⁹. The following derivation applies for area-preserving maps on a 2D plane, but a similar function applies for continuous-time maps and in higher dimensions⁹. For an area-preserving mapping $f(\mathbf{r})$, the Perron-Frobenius operator maps forward densities according to

$$\rho'(\mathbf{r}') = \int d\mathbf{r} \mathcal{L}(\mathbf{r}', \mathbf{r}) \rho(\mathbf{r}), \quad (3)$$

with kernel

$$\mathcal{L}(\mathbf{r}', \mathbf{r}) = \delta(\mathbf{r}' - f(\mathbf{r})), \quad (4)$$

and where ρ is an initial density function over phase space and ρ' is its forward iterate. The escape rate γ is equal to the natural log of the largest eigenvalue λ of \mathcal{L} . One way to compute the leading eigenvalue of \mathcal{L} is to find the zeros of the determinant $\det(1 - z\mathcal{L})$, known as the spectral determinant. The smallest real root z of the spectral determinant greater than 1 yields γ , where $\gamma = -\ln(z)$. The spectral determinant can be written as a power series

$$\det(1 - z\mathcal{L}) = 1 - \sum_{n=1}^{\infty} Q_n z^n, \quad (5)$$

where Q_n are coefficients to be determined. The computation of γ then lies in computing the coefficients Q_n and finding the zeros of Eq. (5). To compute the coefficients Q_n , it helps to take the logarithmic derivative of the spectral determinant. It helps to take the logarithmic derivative of the spectral determinant using

$$\begin{aligned} \text{tr} \left(\frac{z\mathcal{L}}{1 - z\mathcal{L}} \right) &= -z \frac{d}{dz} \ln \det(1 - z\mathcal{L}) \\ &= -\frac{z \frac{d}{dz} \det(1 - z\mathcal{L})}{\det(1 - z\mathcal{L})}. \end{aligned} \quad (6)$$

The left hand side of Eq. (6) can be expanded in a Taylor series in z as

$$\text{tr} \left(\frac{z\mathcal{L}}{1 - z\mathcal{L}} \right) = \sum_{n=1}^{\infty} C_n z^n, \quad (7)$$

where

$$C_n = \text{tr}(\mathcal{L}^n) \quad (8)$$

are known as the trace coefficients. Taking the derivative in Eq. (6) and substituting Eqs. (5) and (7) into Eq. (6) yields the equation

$$\left(1 - \sum_{n=1}^{\infty} Q_n z^n\right) \sum_{m=1}^{\infty} C_m z^m = \sum_{n=1}^{\infty} n Q_n z^n. \quad (9)$$

Equation (9) provides a convenient way to compute the coefficients Q_n in terms of the coefficients C_n . Comparing the coefficients of z on the left and right hand sides of Eq. (9), we see that $Q_1 = C_1$. Similarly, it is easy to prove by induction that

$$Q_n = \frac{1}{n} \left[C_n - \sum_{i=1}^{n-1} Q_i C_{n-i} \right]. \quad (10)$$

The coefficients C_n are defined in Eq. (8) and can be written as

$$C_n = \int d\mathbf{r} \mathcal{L}^n(\mathbf{r}, \mathbf{r}) = \int d\mathbf{r} \delta(\mathbf{r} - f^n(\mathbf{r})). \quad (11)$$

The delta function in Eq. (11) picks up a contribution whenever \mathbf{r} is a fixed point of $f^n(\mathbf{r})$, and so

$$C_n = \sum_{\mathbf{r}_*} \frac{1}{\left| \det(1 - \frac{\partial f^n}{\partial \mathbf{r}} \Big|_{\mathbf{r}_*}) \right|}, \quad (12)$$

where the sum is taken over all fixed points \mathbf{r}_* of f^n . A *prime* periodic orbit is one that is not a copy (or several copies) of a lower-period orbit retracing itself. Equation (12) can be re-written in terms of *prime* orbits as

$$\begin{aligned} C_n &= \sum_p n_p \sum_{r=1}^{\infty} \frac{1}{\left| \det(1 - M_p^r) \right|} \delta_{rn_p, n}, \\ \left| \det(1 - M_p^r) \right| &= \left| (1 - \lambda_p^r) (1 - \lambda_p^{-r}) \right|, \end{aligned} \quad (13)$$

where

$$M_p = \frac{\partial f^{n_p}}{\partial \mathbf{r}} \Big|_{\mathbf{r}_*}, \quad (14)$$

n_p is the period of \mathbf{r}_* , and λ_p is the greater eigenvalue of M_p . The escape rate γ is computed by first computing all prime periodic orbits up to period n and computing the trace coefficients C_n using Eq. (13). Then the coefficients Q_n are computed using Eq. (10). The escape rate γ is then computed by finding the roots of the polynomial in Eq. (5).

One consequence of the spectral determinant for computing γ is that escape from a given region only depends on the periodic orbits in that region, and including or removing regions that have no periodic orbits in them does not change the escape rate.

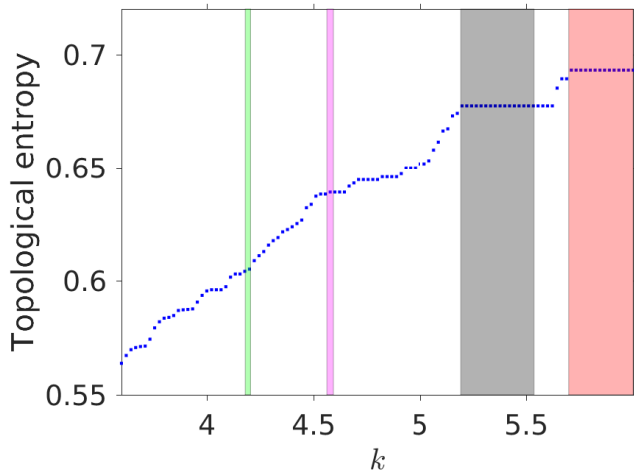


FIG. 1. (Color online) The topological entropy lower bound computed from HLD as a function of k for the area-preserving Hénon map. The vertical bands indicate the parameter ranges whose periodic orbits are computed in Sects. V-VII. The rightmost band (red) marks the k interval $[5.699, \infty)$ where the topological entropy is $\ln(2)$. The grey and magenta bands denote the k intervals $[5.194, 5.5366]$ and $[4.5624, 4.5931]$ respectively, which are both hyperbolic plateaus with topological entropy $\ln(1.969)$ and $\ln(1.895)$ respectively. The green band denotes the interval $[4.1930, 4.201]$ where the inner region is fully hyperbolic. The topological entropy of the inner region for this k interval is exactly half the entropy as the k interval $[4.5624, 4.5931]$.

III. THE AREA-PRESERVING HÉNON MAP

Our model of choice for computing escape rates is the Hénon map³³, given by

$$\begin{aligned}\tilde{x}_{t+1} &= \tilde{y}_t - k + \tilde{x}_t^2, \\ \tilde{y}_{t+1} &= -b\tilde{x}_t,\end{aligned}\quad (15)$$

where k and b are parameters of the map. We plot the figures in this paper using rotated coordinates $x = (\tilde{x} - \tilde{y})/\sqrt{2}$, $y = (\tilde{x} + \tilde{y})/\sqrt{2}$, so that the symmetry axis is horizontal. We define M as the map which evolves a point $\mathbf{r}_t = (x_t, y_t)$ forward to the point $\mathbf{r}_{t+1} = (x_{t+1}, y_{t+1})$. Although the techniques discussed throughout this paper are valid for maps that are not area-preserving, we require area-preservation here ($b = 1$) to connect with Hamiltonian dynamical systems. Given $b = 1$, M can exhibit a variety of chaotic behavior ranging from a complete binary horseshoe at $k > 5.699$ to a mixed phase space with stable islands embedded in a chaotic sea at lower k values.

Figure 1 shows the topological entropy of the Hénon map computed over a range of k values using symbolic dynamics computed from HLD. The rightmost shaded band denotes the k interval $[5.699, \infty)$ where the dynamics exhibits a complete horseshoe with topological entropy of $\ln(2)$. As k is lowered, the topological entropy decreases monotonically. This decrease is not

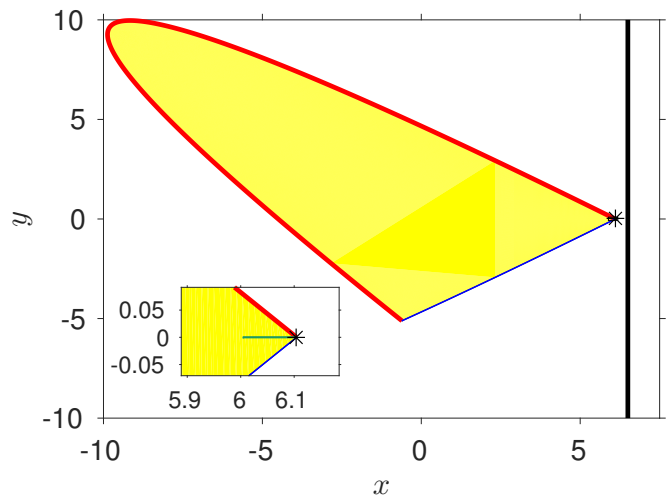


FIG. 2. (Color online) The resonance zone (yellow) for $k = 10$. The asterisk marks the location of the fixed point whose stable (red) and unstable (blue) manifolds bound the resonance zone. The vertical line used to define escape for MC simulations is shown in black. The initial ensemble of points for MC simulations is shown in green.

strictly monotonic because of the existence of hyperbolic plateaus, which are intervals of k where the dynamics is hyperbolic and the topological entropy does not change. The grey and magenta bands denote the intervals of k that Arai identified as hyperbolic plateaus³⁴, namely $[5.194, 5.5366]$ and $[4.5624, 4.5931]$. The green band denotes an interval of k where a subregion of phase space exhibits exactly half the entropy as the plateau shown in magenta. In this case, the subregion exhibits a hyperbolic plateau when treated as its own dynamical system.

IV. MONTE CARLO COMPUTATION OF ESCAPE RATE

Throughout this study, we compute the escape rate γ using an MC method to compare with the value obtained from periodic orbits. The phase portrait for $k = 10$ is shown in Fig. 2. The resonance zone (yellow) is bounded by the stable and unstable manifolds of a hyperbolic fixed point, and contains all of the periodic orbits in the system. Escape from the resonance zone is defined by leaving the zone and entering the unbounded white region. Alternatively, escape can be defined as passing to the right of the vertical line in Fig. 2. Both definitions give exactly the same escape rate since no periodic orbits exist outside the resonance zone. The initial points, shown in green in Fig. 2, are chosen near the fixed point. Due to ergodicity, the exact choice of initial ensemble does not affect the decay rate. Figure 3 shows the number of surviving trajectories along with the fit line whose slope gives the approximation to the escape rate. Here the vertical line is used as the escape criterion. Depending on available computational resources

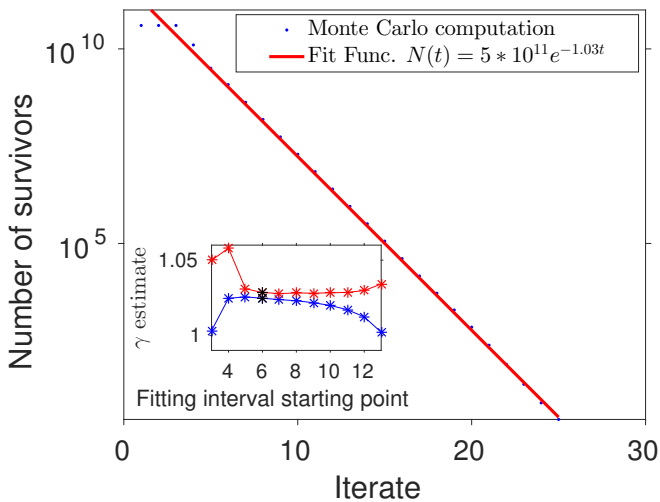


FIG. 3. (Color online) The number of surviving (blue dots) trajectories as a function of iterate for $k = 10$. The fitting function (red) is fit to the iterate interval $[6, 20]$. The escape rate computed from this fit is 1.02814 ± 0.00071 . Inset: The escape rate upper (red) and lower (blue) bounds as a function of fit interval. The end point of the fit interval is 20 iterates. The error bounds chosen for comparison with periodic orbits are shown in black.

at the time of study, the MC simulations were either run using the Message Passing Interface (MPI)³⁵ on the Multi-Environment Research Computer for Exploration and Discovery (MERCED) using 25 20-Core Xeon E5 2650v4 nodes, or using the Compute Unified Device Architecture (CUDA)³⁶ on an NVIDIA GTX 970 graphics processing unit. Appendix A describes the fitting method used and the choice of error bounds based on the goodness of fit.

In the case of multiexponential escape, as in Eq. (2), choosing an initial ensemble just outside the resonance zone is more suitable. Starting the initial points outside the resonance zone gives more time for transients to expire before the points begin to escape, allowing for a more accurate observation of the fast, initial escape rate. Such a computation of escape also mimics the scattering of electrons from nuclei in chaotic atomic systems, as studied in Refs.^{37,38}. After iterating the initial points forward they enter the resonance zone before escaping past the vertical line. For $k = 4.1933$, the escape curve is biexponential, as shown in Fig 4, exhibiting a fast, initial escape rate and then a slow, secondary escape rate. We compute the two escape rates for $k = 4.1933$ using periodic orbits in Sect. VII.

V. ESCAPE FOR A FULL SHIFT ON TWO SYMBOLS

We first demonstrate the spectral determinant technique for $k > 5.699$, where the dynamics is a complete binary horseshoe. The dynamics can be encoded using two symbols denoted 0 and 1, whose corresponding par-

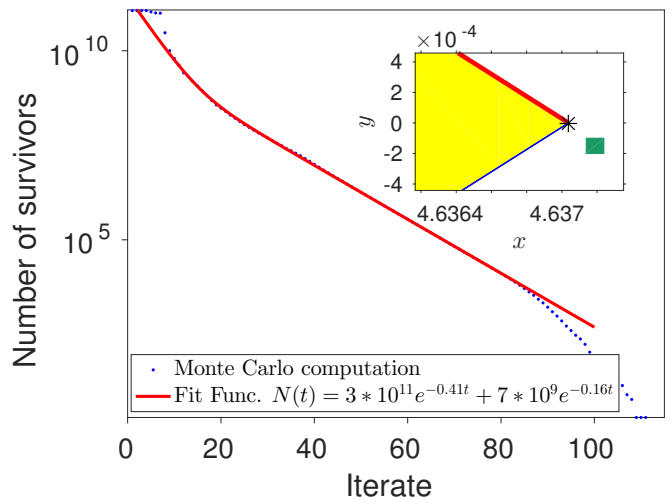


FIG. 4. (Color online) The number of surviving trajectories as a function of iterate for $k = 4.1933$, using initial points outside the resonance zone. The secondary escape rate is computed first by taking a natural log of the data and fitting a line to the interval starting at iterate 52 and ending at iterate 80. The short-time escape rate is then computed by subtracting the resulting fitting function from the data and fitting to the interval starting at iterate 13 and ending at iterate 24. Inset: The phase portrait near the fixed point for $k = 4.1933$. The asterisk marks the location of the fixed point whose stable (red) and unstable (blue) manifolds bound the resonance zone. The initial ensemble of MC points is shown in green. Details of computing the fitting function are described in Appendix A.

tition domains are shown for $k = 10$ in Fig. 5. The symbolic dynamics transition graph is shown in the inset of Fig. 5. All periodic orbits in the system consist of points lying in region 0 and region 1, and the symbolic itinerary of any period- N orbit is a binary string of length N .

A. Periodic orbit computation of γ

An accurate partitioning of the phase space and corresponding symbolic dynamics allows for characterizing and computing periodic orbits in order to compute γ from the spectral determinant. The symbolic dynamics is used to generate a symbolic itinerary for a given periodic orbit. The symbolic itinerary along with the corresponding partition domains are used to construct a seed. The seed is then used in a multi-point shooting method to compute the periodic orbit. Appendix B explains how to generate accurate seeds using the boundaries of the partition domains and how to compute periodic orbits. Once the periodic orbits are computed, the eigenvalue λ_p of each orbit is computed from the explicit linearization of Eq. (15). The values of λ_p and their corresponding periods are used to construct the spectral determinant and find the zeros of Eq. (5). The escape rate computed from periodic orbits becomes more accurate as higher-period

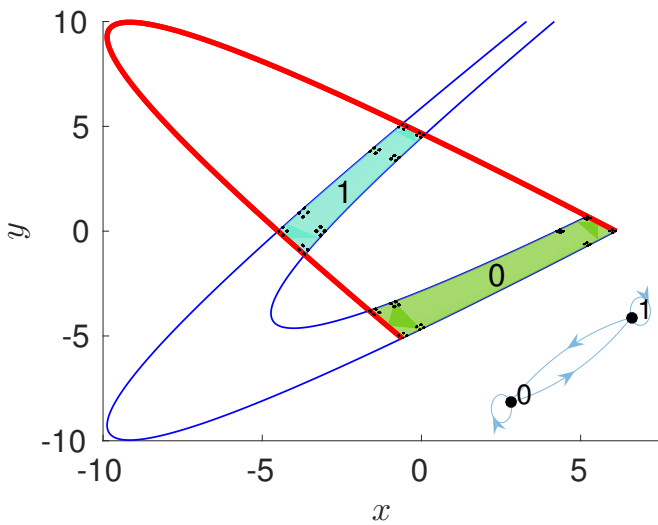


FIG. 5. (Color online) $k = 10$ partition domains. The periodic orbits up to period 13 are plotted in black. The symbolic dynamics (inset) is a full shift on two symbols.

Period	Cumulative number of orbits	γ
1	2	1.1989476364
2	3	0.99036961
3	5	1.0371111058
4	8	1.0274997079
5	14	1.0278413650
6	23	1.0279897430
7	41	1.0280053653
8	71	1.0280053619
9	127	1.0280053745
10	226	1.0280053736
11	412	1.0280053736
12	747	1.0280053734
13	1337	1.0280053742
Monte Carlo		1.02814 ± 0.00071

TABLE I. The cumulative number of periodic orbits used up to the given period and the value of γ computed from the spectral determinant up to that period for $k = 10.0$. The error bound for the MC method is computed using the 95% confidence interval from the fit.

orbits are used, as shown in Fig. 6 and Table I.

Once periodic orbits are computed for a given value of k , they can be used as seeds for computing orbits for a nearby k value, because a small change in k results in a small change in the locations of the periodic orbits. Thus, k can be varied iteratively and periodic orbits can be computed over a range of parameter values, which is a technique known as periodic orbit continuation. The periodic orbits are then used to compute the escape rate from the spectral determinant. Periodic orbits that disappear or become stable in a bifurcation as k is lowered are removed from the spectral determinant computation.

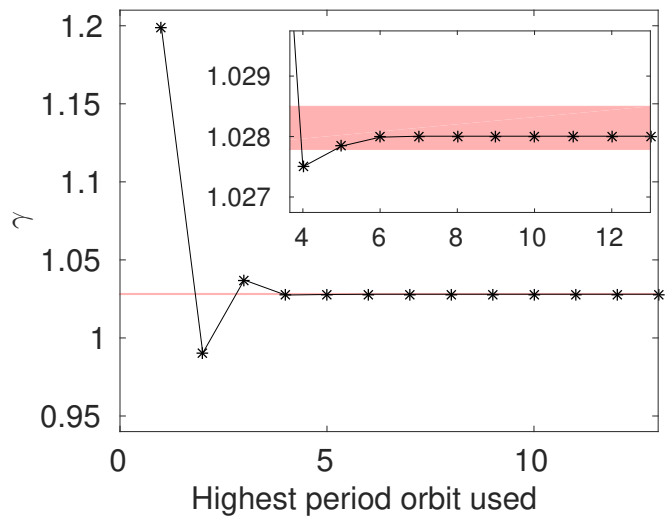


FIG. 6. (Color online) Escape rate versus period for $k = 10$ using the spectral determinant (black). The red band is the MC 95% confidence interval 1.02814 ± 0.00071 . Due to strong hyperbolicity for this k value, the periodic orbit escape rate converges exponentially to the MC value as a function of the highest period orbit used.

Figure 7 shows the escape rate as a function of k for the interval $[5.1, 10.0]$ using both MC and periodic orbit methods. Below $k = 5.699$, the phase space no longer exhibits a complete binary horseshoe, and periodic orbits begin to bifurcate. The spectral determinant computation accurately matches the MC value for the entire interval shown in Fig. 7, however, as k falls below $k = 5.699$, the computation requires more orbits to accurately match the MC computation, as shown in the fluctuations in the spectral determinant computation at lower period below $k = 5.699$ in the inset of Fig. 7.

VI. ESCAPE OVER HYPERBOLIC PLATEAUS

As k is lowered, the Hénon system no longer exhibits a full binary symbolic dynamics.

A. Computing periodic orbits with HLD

When k is less than 5.699, the topological entropy begins to fall below $\ln(2)$ as periodic orbits are lost in bifurcations. We employ a technique called Homotopic Lobe Dynamics^{17,18} (HLD) to compute the system's symbolic dynamics and the corresponding partition. This automated technique uses information encoded in the intersections of finite-length segments of stable and unstable manifolds of periodic orbits. In the HLD technique, the stable and unstable manifolds of the anchor periodic orbit are first computed up to a primary intersection point²³. Then pieces of the unstable manifold are iterated forward a finite number of times, and the symbolic dynamics is

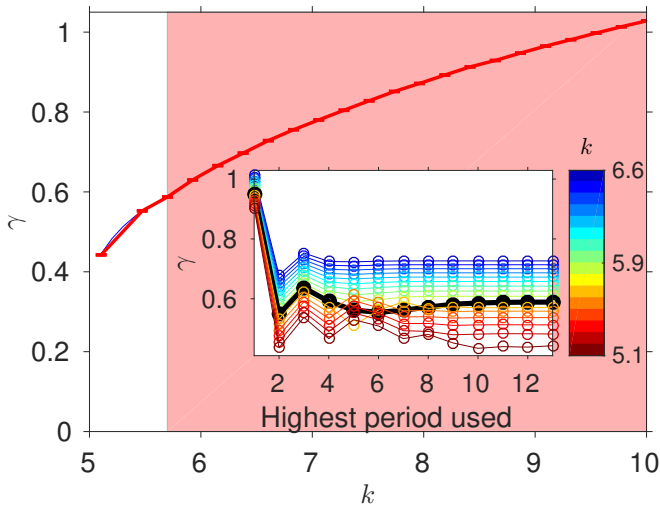


FIG. 7. (Color online) The MC (red) and spectral determinant (blue) escape rates as a function of k for $k \in [5.1, 10]$. The two curves lie almost on top of each other. Above $k = 5.699$ (red band), the symbolic dynamics is a full shift on two symbols and all periodic orbits up to period 13 are used in the computation of γ . As k is lowered past 5.699, periodic orbits that disappear or become stable in a bifurcation are removed from the spectral determinant computation. Inset: The spectral determinant escape rate computed as a function of period for the k range $[5.1, 6.6]$, specified by the colorbar. The escape rate for the bifurcation point, $k = 5.699$, is plotted in black.

extracted from the intersections of the stable and unstable manifolds. The finite-length segments of stable and unstable manifolds used for computing HLD are known as a *trellis*; a trellis for $k = 5.4$ is shown in Fig. 8a. The resulting symbolic dynamics computed from HLD is shown in Fig. 8b and a schematic representation of the corresponding partition is shown in Fig. 8c. The periodic orbits are computed from the partition as described in Sect. V and Appendix B, and are shown in Fig. 9.

B. Computing escape rates with periodic orbits

We now focus on two fully hyperbolic intervals of k whose rigorous bounds were identified by Arai³⁴, namely $[5.194, 5.5366]$ and $[4.5624, 4.5931]$. Such hyperbolic intervals of k are useful for computing escape rates from periodic orbits because no orbits are lost or created in bifurcations as k is varied over the interval. Once periodic orbits are computed for a given k value within a hyperbolic plateau, they can be computed for the entire interval using periodic orbit continuation. Figure 10 shows the escape rate as a function of the highest period orbit used using the spectral determinant for $k = 5.4$, chosen near the center of the hyperbolic plateau. The escape rate is then computed for $k \in [5.194, 5.5366]$ using periodic orbit continuation, shown in Fig. 11a. The same process is used to compute the escape rate for the interval

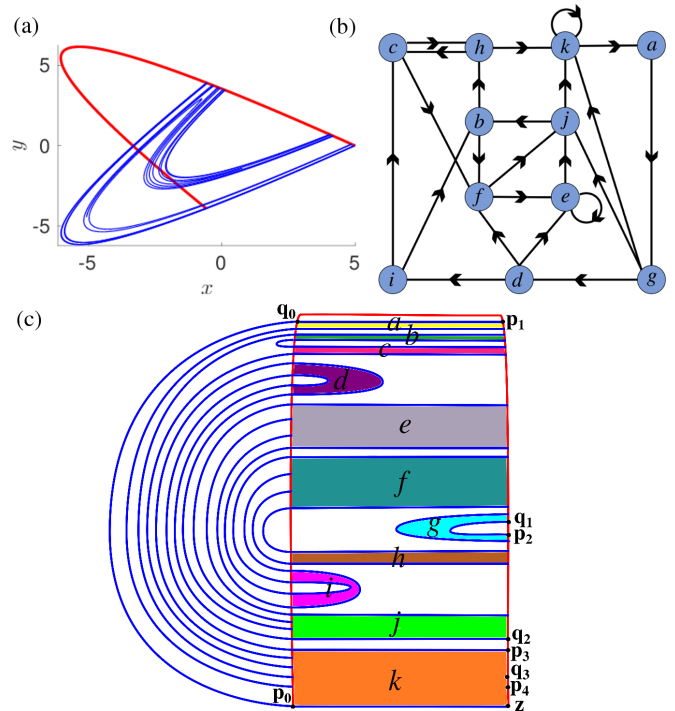


FIG. 8. (Color online) (a) The trellis for $k = 5.4$. (b) The transition graph computed from HLD. (c) A schematic representation of the corresponding partition.

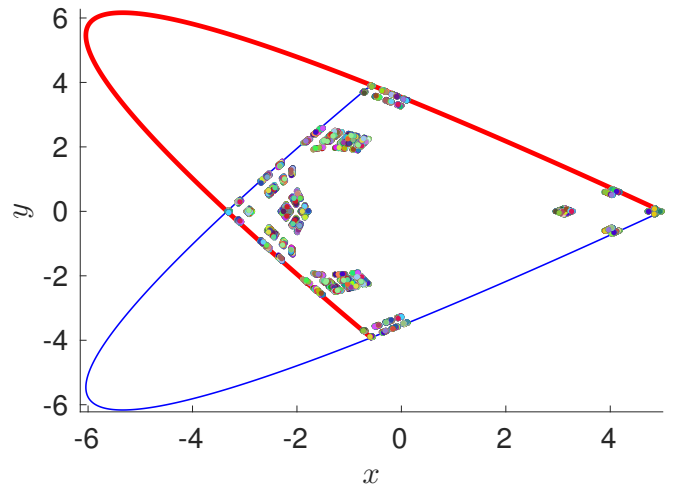


FIG. 9. (Color online) All periodic orbits up to period 13 for $k = 5.4$.

$[4.5624, 4.5931]$. The periodic orbits are first computed for $k = 4.575$ using HLD, then periodic orbit continuation is used to compute the escape rate over the entire interval, shown in Fig. 11b. For both hyperbolic plateau intervals, the escape rate computed from periodic orbits accurately predicts the MC escape rate within the hyperbolic plateau. As k is lowered below the hyperbolic plateau bound, periodic orbits that become stable or are lost in a bifurcation begin to distort the periodic orbit computation of γ , and the periodic orbit estimate begins

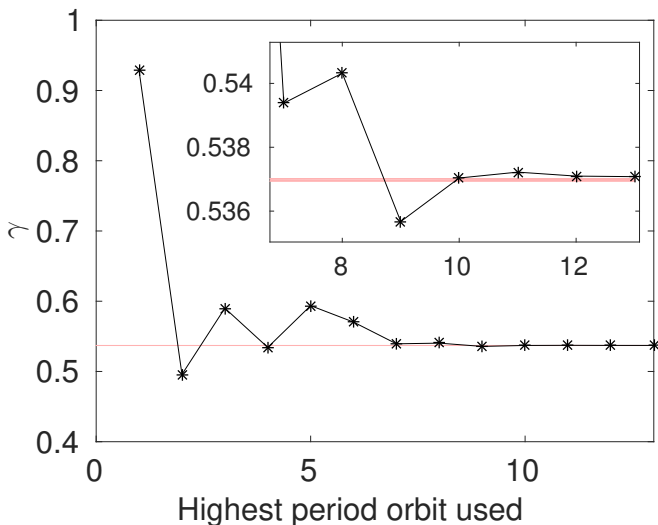


FIG. 10. (Color online) Escape rate versus period for $k = 5.4$ computed from periodic orbits (black) and MC simulation (red band).

to vary from the MC value. The escape rate goes to zero every time a periodic orbit bifurcates, which causes the dips in the blue data in Fig. 11(a). In Fig. 11(b), none of the periodic orbits computed at $k = 4.575$ bifurcate in the interval shown. As k is increased above the hyperbolic plateau bound, orbits that exist at the higher k value are not accounted for, and therefore the periodic orbit estimate of the escape rate becomes less accurate.

VII. MULTIEXPONENTIAL ESCAPE RATES

For the k values studied in Sects. V and VI, the dynamics exhibits a single exponential escape rate as in Eq. (1). More complicated phase spaces can exhibit multiexponential escape rates as in Eq. (2) and as shown for $k = 4.1933$ in Fig. 4. The inset of Fig. 12 shows the phase portrait at $k = 4.1933$, which exhibits three distinct zones: Zone 0 (white), Zone I (yellow), and Zone II (red). Zone II is bounded by the stable and unstable manifolds of an inner fixed point with inversion, meaning it has a negative eigenvalue. All periodic orbits within Zone II, except for the fixed point, have an even period. Although the inner period-two structure in Zone II persists at $k > 4.28$, the boundary of Zone II intersects the boundary of Zone I, and it becomes difficult to distinguish two distinct escape rates.

A. Inner hyperbolic plateaus

Zone II in Fig. 12 can be treated as its own dynamical system, which exhibits its own hyperbolic plateaus. Using HLD applied to the stable and unstable manifolds of the inner fixed point, we identified a parameter value

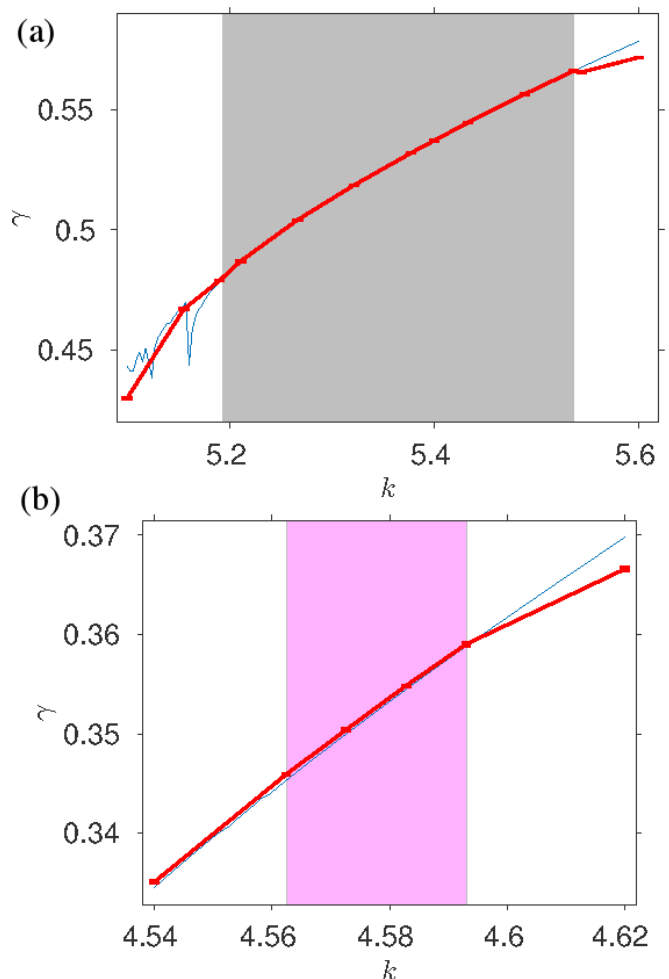


FIG. 11. (Color online) Escape rates computed using the spectral determinant (blue) and MC simulation (red) versus k for (a) $k \in [5.1, 5.6]$ and (b) $k \in [4.54, 4.62]$. The shaded bands denote the hyperbolic plateaus $[5.194, 5.5366]$ (grey) and $[4.5624, 4.5931]$ (magenta).

$k = 4.3$ for which the topological entropy of Zone II is exactly half the topological entropy of the full phase space over the plateau $[5.194, 5.5366]$. Moreover, the HLD symbolic dynamics of the bottom half of M^2 in Zone II is identical to the HLD symbolic dynamics of the full phase space under M for $k \in [5.194, 5.5366]$.

Unfortunately, we did not detect a strong secondary exponential decay at $k = 4.3$. Thus we searched for a hyperbolic plateau for Zone II with exactly half the topological entropy as the full phase space for $k \in [4.5624, 4.5931]$, the lower hyperbolic plateau studied in Sect. VI. The interval $k \in [4.1930, 4.201]$ was found to have this topological entropy, and furthermore the bottom half of Zone II under M^2 has the same HLD symbolic dynamics as $k \in [4.5624, 4.5931]$ under M . The topology of the inner trellis remains the same over this interval and therefore there are no bifurcations in periodic orbits within the inner zone. The trellis at $k = 4.1933$, near the center of the plateau, is used to compute the HLD, the

	Starting Zone, Escape Zone	PO	Monte Carlo
γ_I	I, $0 \cup \text{II}$	0.3781	$0.35823 \pm 5e-5$
γ_{II}	II, $0 \cup \text{I}$	0.18039	$0.18245 \pm 3e-5$
$\gamma_{I,II}$	II, 0	0.16512	$0.16406 \pm 2e-5$

TABLE II. Summary of the three escape rates γ_I , γ_{II} , and $\gamma_{I,II}$ along with the periodic orbit and MC escape rate computations for $k = 4.1933$.

partition, and the periodic orbits.

B. Monte Carlo computations for nested zones

Unlike Sects. V and VI, where a vertical line is used to define escape, the escape criterion for the nested zones is based on the boundaries of individual resonance zones. The initial points are chosen to be uniformly distributed in a particular zone, and the escape criterion is defined as entering a different zone. The zone in which a particular point lies is determined using a point-in-polygon test. As points are mapped forward, their zone is computed and the number of surviving trajectories is counted as a function of iterate. For phase spaces such as the inset of Fig. 12, three distinct escape rates can be computed as summarized in Table II: escape from Zone I, escape from Zone II, and escape from the union of Zones I and II, labeled as γ_I , γ_{II} , and $\gamma_{I,II}$ respectively. The escape rate γ_I is computed by choosing the initial points in Zone I and defining escape as entering Zones II or 0. The escape rate γ_{II} is computed by choosing initial points in Zone II defining escape as entering Zones I or 0. The escape rate $\gamma_{I,II}$ can be computed by choosing initial points in the union of Zone I and Zone II and defining escape as entering Zone 0. In this case, since Zone II has the slowest escape rate, $\gamma_{I,II}$ will be dominated by the points starting in Zone II. Therefore $\gamma_{I,II}$ is computed more accurately by choosing initial points in Zone II and defining escape as entering Zone 0. The MC curves for γ_I , γ_{II} , and $\gamma_{I,II}$, including the two different ways of computing $\gamma_{I,II}$, are shown in Fig. 12. The resulting escape rates computed from MC are shown in Table II.

Comparing the results in Table II to the MC simulation and bi-exponential fit in Fig. 4, the slow escape rate in Fig. 4 matches the MC escape rate $\gamma_{I,II}$, and the fast escape rate in Fig. 4 is quite close to γ_I . This is because the fast, initial escape rate in Fig. 4 is due to points that initially escape from Zone I, and the slower, secondary escape rate is due to points that stay in Zones I and II longer and eventually escape.

C. Nested trellis

An important advantage of the HLD technique is the ability to target individual regions of phase space by including the stable and unstable manifolds of additional

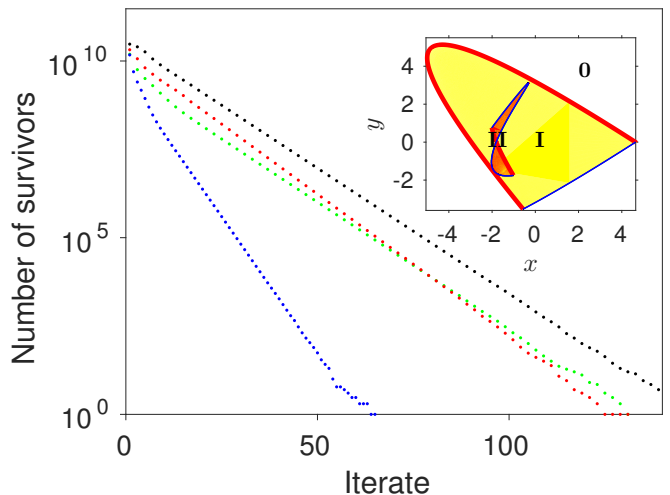


FIG. 12. (Color online) MC escape rates for different zones for $k = 4.1933$. The initial points are chosen uniformly from the starting zone, and escape occurs when a point enters the escape zone. In green, the MC escape rate for $\gamma_{I,II}$ is computed using Zone II as the starting zone and the union of Zone I and Zone 0 as the escape zone. In black, a different computation for $\gamma_{I,II}$ is computed using initial points in Zone II and defining escape as entering Zone 0. The green and black lines are parallel, but the black line yields a better estimate for the value $\gamma_{I,II}$, because the MC simulation for the green data includes points in the outer zone, which have a faster initial escape, while the black line levels off more quickly. In blue, the MC escape rate for γ_I is computed, using initial points distributed uniformly in Zone I and defining escape as entering Zone II or Zone 0. In red, the MC escape rate γ_{II} is computed using initial points distributed uniformly in Zone II and defining escape as entering Zone I or Zone 0. Inset: The two resonance zones. We denote the unbounded white region as Zone 0, the bounded yellow region as Zone I, and the inner bounded red region as Zone II.

periodic orbits, creating a nested trellis¹⁸. This technique can be used to target Zones I and II in the inset of Fig. 12. To target Zone I, the stable and unstable manifolds of the outer fixed point are used, as in Sects. V and VI. To target Zone II, the stable and unstable manifolds of the inner fixed point with inversion are also included. The resulting trellis is shown in Fig. 13a. The additional heteroclinic intersections included in the nested trellis lead to a better sampling of the topology of phase space, compared to using the outer trellis alone. Using the nested trellis results in a more accurate symbolic dynamics for the full phase space, whose transition graph contains 351 nodes and 645 edges. The corresponding partition computed from HLD is shown in Fig. 13b. The periodic orbits computed from the partition domains are shown in Fig. 13c.

From the nested trellis, three different transition matrices are obtained. T_I is the transition matrix for Zone I, T_{II} is the transition matrix for Zone II, and $T_{I,II}$ is the transition matrix for the union of Zones I and II. The transition matrix $T_{I,II}$ contains all the nodes and edges

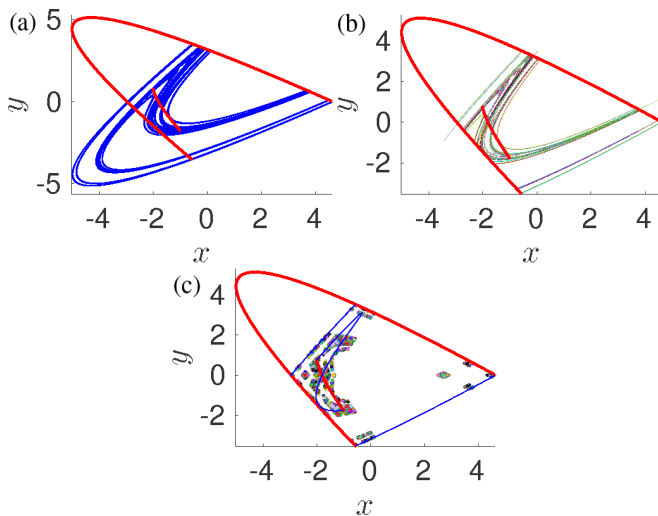


FIG. 13. (Color online) (a) Full trellis for $k = 4.1933$. (b) The partition for $k = 4.1933$. Some partition domains computed from HLD make additional intersections with the stable manifold and extend outside the resonance zone. This is due to additional structure in the trellis that is not detected by initial computation of symbolic dynamics using HLD¹⁸. (c) All periodic orbits up to period 14 for $k = 4.1933$.

in T_I and in T_{II} , but it also contains additional edges that connect Zones I and II. It does not contain any additional nodes, as all nodes lie in either Zone I or Zone II. The topological entropies of T_I , T_{II} , and $T_{I,II}$ are $\ln(1.8311)$, $\ln(1.3766)$, and $\ln(1.8390)$ respectively. The topological entropy of Zone II at $k = 4.1933$ is exactly half that of the full phase space at $k \in [4.5624, 4.5931]$.

D. Periodic orbits and spectral determinants for nested zones

To compute the escape rate from a given zone using the spectral determinant, we include only periodic orbits from that zone. The escape rate γ_I is the escape from Zone I, and therefore γ_I is computed using periodic orbits that lie only in Zone I, computed from T_I . The escape rate γ_{II} is the escape rate from Zone II, and therefore γ_{II} is computed using only periodic orbits that lie only in Zone II, computed from T_{II} . The escape rate $\gamma_{I,II}$ is the escape rate from both zones, and therefore $\gamma_{I,II}$ is computed using all periodic orbits, computed from $T_{I,II}$. The three distinct escape rates computed with periodic orbits and MC simulations are shown in Fig. 14 and Table II. Targeting the inner region and capturing its full topology using HLD allows for computing all periodic orbits up to period 20, which yields an accurate value for the escape rate γ_{II} (red). Using the nested trellis approach with the stable and unstable manifolds from both resonance zones also yields an accurate result of the escape rate $\gamma_{I,II}$ (black), even though our computation of HLD has not extracted the exact symbolic dynamics, and

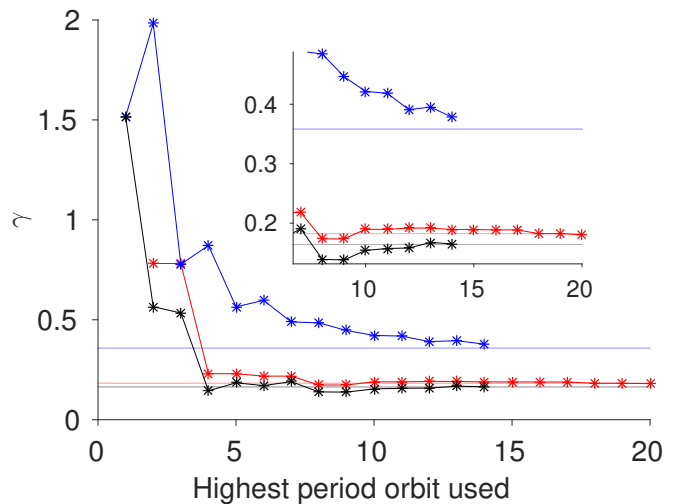


FIG. 14. (Color online) The periodic orbit and MC computations of γ_I (blue), γ_{II} (red) and $\gamma_{I,II}$ (black) using periodic orbits (lines with asterisks) and MC simulation (horizontal bands) for $k = 4.1933$.

some periodic orbits may be missing from the computation. The outer escape rate γ_I (blue) is the least accurate, which means some periodic orbits are missing from the HLD computation, or more orbits of higher period are required to accurately obtain the escape rate. Figure 15 shows the escape rates computed as a function of k using periodic orbit continuation, along with the corresponding MC escape rates. The inner escape rate γ_{II} is computed accurately over the entire interval. The escape rate for both zones, $\gamma_{I,II}$, is computed most accurately at the k value where HLD is computed, $k = 4.1933$, and captures part of the variation in escape rate as k is varied. The escape rate from the outer zone γ_I is computed less accurately over this k range. Finally, note that errors on the escape rates γ_I , γ_{II} , and $\gamma_{I,II}$ are smaller than the differences between the rates.

VIII. CONCLUDING REMARKS

Single-exponential and multi-exponential escape rates can be reliably computed using periodic orbits from HLD in lieu of an MC simulation requiring tens of billions of orbits. Unlike MC simulations, which require the computation of large numbers of trajectories at each parameter value where escape rates are computed, periodic orbit continuation allows for accurate computation of escape rates over a range of parameter values once the periodic orbits are found for a particular parameter value. The result of HLD is particularly accurate within hyperbolic plateaus where no periodic orbits bifurcate. By finding a parameter range where an inner resonance zone exhibits a hyperbolic plateau, we use periodic orbits from HLD to compute distinct, multiexponential escape rates from different resonance zones.

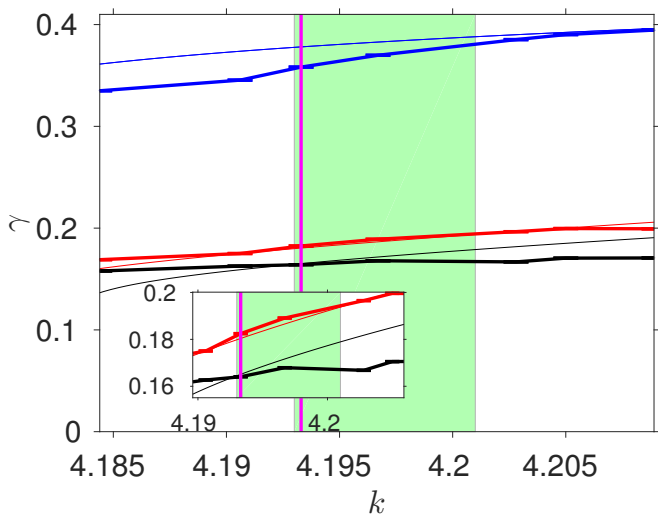


FIG. 15. (Color online) The escape rates γ_I (blue), γ_{II} (red), and $\gamma_{I,II}$ (black) computed as a function of k using MC (bold with error bars) and with periodic orbits (finer line with no markers). Once an orbit becomes stable or is lost in a bifurcation, it is removed from the spectral determinant calculation for all lower k values. The vertical magenta line denotes $k = 4.1933$, the value at which HLD was computed to compute the periodic orbits.

ACKNOWLEDGMENTS

The authors acknowledge the support of the U.S. National Science Foundation under Grant No. PHY-1408127 and the East Asia and Pacific Summer Institutes (EAPSI) grant No. EAPSI-1614377. MC simulations were computed on the Multi-Environment Research Computer for Exploration and Discovery (MERCED), which is supported by the National Science Foundation Grant No. ACI-1429783. We thank Hrant Hrachian, Suzanne Sindi, Jeffrey Weekley, and Sarvani Chadalapa for their patient assistance in helping us use the MERCED cluster. We gratefully acknowledge research discussions with Zin Arai, Tamiki Komatsuzaki, Mikito Toda, and Hiroshi Teramoto.

Appendix A: Choosing appropriate fit intervals and error bounds for Monte Carlo escape rates

Once the MC data shown in Fig. 3 (blue) is computed by counting the number of surviving trajectories as a function of time, the escape rate is computed by fitting a line to the log of this data. The starting and ending iterates for the fit interval must however be carefully chosen to obtain an accurate bound on the escape rate. If the starting iterate of the fit interval is too low, the transients will not have expired, and correlated trajectories that escape in the first several iterates will provide an inaccurate result for the escape rate. If the starting iterate of the fit interval is too high, there will be too few points remaining

in the simulation to properly sample the phase space and resolve the escape rate of the system. If the end point of the fit interval is too low, the data at later iterates is not being utilized, and the accuracy of the escape rate computation is compromised. If the end point of the fit interval is too high, then later iterates, which have low statistics, will throw off the accuracy of the escape rate. To get around this issue, the fit is computed over every possible starting and ending point value, and the starting and ending point with the tightest confidence interval is chosen. The inset of Fig. 3 shows the escape rate upper and lower bounds computed as a function of the starting point of the fit interval by fixing the ending point of the fit interval at 25. The escape rate estimates are wider for the first few iterates, then they level off and remain flat, but at even later iterates the error bars eventually grow large when the remaining number of surviving trajectories is low. The smallest error bounds shown in black are chosen. This technique is used for computing all MC escape rates in Sects. V-VII.

In the case of the scattering problem studied in Fig. 4, the bi-exponential escape rate is computed by first fitting an exponential to the later iterates to extract the secondary decay, then subtracting that fit function from the data, and finally fitting to the earlier iterates of the data to compute the initial decay.

Appendix B: Method to compute periodic orbits

The computation of periodic orbits from Newton's method requires an initial guess. The HLD technique allows for choosing an initial guess based on partition domains and symbolic dynamics. Each periodic orbit has a symbolic itinerary representing it, and the initial guess for each point in a symbolic itinerary is chosen as the center of the partition domain with the corresponding symbol. For example, for the full shift on two symbols, every periodic orbit can be labeled using a sequence of 0's and 1's. The two labels correspond to the partition domains shown in Fig. 5. The center of each partition domain is used as a seed. The seed points are then used in Newton's method to solve an equation of the form

$$\begin{pmatrix} M(\mathbf{r}_1) - \mathbf{r}_2 \\ M(\mathbf{r}_2) - \mathbf{r}_3 \\ \vdots \\ M(\mathbf{r}_{n-1}) - \mathbf{r}_n \\ M(\mathbf{r}_n) - \mathbf{r}_1 \end{pmatrix} = \begin{pmatrix} 0 \\ 0 \\ \vdots \\ 0 \\ 0 \end{pmatrix} \quad (\text{B1})$$

where \mathbf{r}_i are the points in the periodic orbit of period n . For example the unknown periodic orbit whose itinerary is 010 consists of a sequence of three unknown points $\mathbf{r}_1\mathbf{r}_2\mathbf{r}_3$. The equation to solve using Newton's becomes

$$\begin{pmatrix} M(\mathbf{r}_1) - \mathbf{r}_2 \\ M(\mathbf{r}_2) - \mathbf{r}_3 \\ M(\mathbf{r}_3) - \mathbf{r}_1 \end{pmatrix} = \begin{pmatrix} 0 \\ 0 \\ 0 \end{pmatrix}. \quad (\text{B2})$$

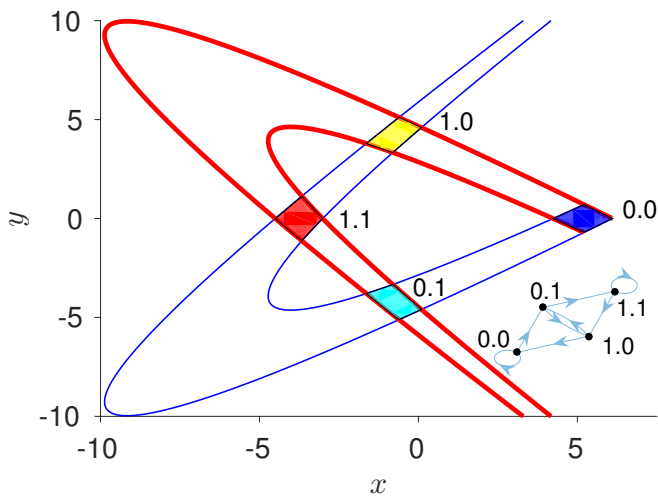


FIG. 16. (Color online) A refinement of the full shift on two symbols. The extended stable manifold (red) cuts the partition domains for 0 and 1 into four new partition domains representing the two-symbol strings 0.0, 0.1, 1.0, and 1.1. This symbolic dynamics generates the same periodic orbits and therefore has the same topological entropy of $\ln(2)$ as the full shift on two symbols.

Since the symbolic itinerary of this example orbit is 010, the initial guess in Newton's method is the sequence of points $\mathbf{r}_1\mathbf{r}_2\mathbf{r}_3 = \mathbf{s}_0\mathbf{s}_1\mathbf{s}_0$, where \mathbf{s}_0 is the center of partition domain 0 and \mathbf{s}_1 is the center of the partition domain 1.

For some higher-period orbits, using the centers of the original partition domains is not sufficient to compute periodic orbits, i.e. the seed point does not converge to the correct periodic orbit under Newton's method. In this case, we refine the partition domains to select a more accurate seed. Since the partition domains are bounded by segments of stable and unstable manifolds, they can be cut into smaller partitions by mapping the boundaries of the partition domains forward or backward to cut them into smaller portions. Adding symbols on the right refines the partition domain by iterating the stable manifold backward; adding symbols on the left refines the partition domains by iterating the unstable manifold forward. For example, for the full shift on two symbols, one can cut the partition domains 0 and 1 in Fig. 5 into four partition domains, 0.0, 0.1, 1.0, and 1.1 in Fig. 16, where 0.0 represents a point that is in 0 now and maps to 0 in the future, and 0.1 represents a point that is in 0 now and maps to 1 in the future, and so on. The seed point for the period-three orbit 010 now becomes $\mathbf{s}_{0.1}\mathbf{s}_{1.0}\mathbf{s}_{0.0}$. This seed is more likely to converge to the desired periodic orbit. The symbolic dynamics expressed in terms of the symbols $\{0.0, 0.1, 1.0, 1.1\}$ is isomorphic to the original symbolic dynamics. In this manner, the partition domains can be refined for arbitrarily long symbol strings by iterating the stable or unstable manifold more and more times. The boundaries of partition domains that have longer stable or unstable segments can

be mapped backward or forward to form a more balanced partition domain, which effectively moves the dot in the direction that the partition domain is being mapped.

- ¹C. Jaffé, S. D. Ross, M. W. Lo, J. Marsden, D. Farrelly, and T. Uzer, *Phys. Rev. Lett.* **89**, 011101 (2002).
- ²T. Uzer, C. Jaffé, J. Palacián, P. Yanguas, and S. Wiggins, *nonlinearity* **15**, 957 (2002).
- ³J.-L. Thiffeault and M. D. Finn, *Philosophical Transactions of the Royal Society of London A: Mathematical, Physical and Engineering Sciences* **364**, 3251 (2006).
- ⁴H. Teramoto, M. Toda, M. Takahashi, H. Kono, and T. Komatsuzaki, *Phys. Rev. Lett.* **115**, 093003 (2015).
- ⁵S. Sattari, Q. Chen, and K. A. Mitchell, *Chaos: An Interdisciplinary Journal of Nonlinear Science* **26**, 033112 (2016).
- ⁶M. C. Gutzwiller, *Journal of Mathematical Physics* **12** (1971).
- ⁷M. C. Gutzwiller, *Chaos in Classical and Quantum Mechanics* (Springer, New York, 1990).
- ⁸P. Cvitanović and B. Eckhardt, *Phys. Rev. Lett.* **63**, 823 (1989).
- ⁹P. Cvitanović, R. Artuso, R. Mainieri, G. Tanner, and G. Vattay, *Chaos: Classical and Quantum* (Niels Bohr Institute, Copenhagen, 2010) ChaosBook.org.
- ¹⁰A. Holle, G. Wiebusch, J. Main, B. Hager, H. Rottke, and K. Welge, *Phys. Rev. Lett.* **56**, 2594 (1986).
- ¹¹J. Main, G. Wiebusch, A. Holle, and K. Welge, *Phys. Rev. Lett.* **57**, 2789 (1986).
- ¹²A. Holle, J. Main, G. Wiebusch, H. Rottke, and K. Welge, *Phys. Rev. Lett.* **61**, 161 (1988).
- ¹³M. Du and J. Delos, *Phys. Rev. A* **38**, 1896 (1988).
- ¹⁴M. Du and J. Delos, *Phys. Rev. A* **38**, 1913 (1988).
- ¹⁵J. Main, G. Wiebusch, K. Welge, J. Shaw, and J. Delos, *Phys. Rev. A* **49**, 847 (1994).
- ¹⁶D. Kleppner and J. B. Delos, *Foundations of Physics* **31**, 593 (2001).
- ¹⁷K. A. Mitchell, *Physica D* **238**, 737 (2009).
- ¹⁸K. A. Mitchell, *Physica D: Nonlinear Phenomena* **241**, 1718 (2012).
- ¹⁹P. Collins, *Int. J. Bifurcation Chaos Appl. Sci. Eng.* **12**, 605 (2002).
- ²⁰P. Collins, *Dyn. Syst.* **19**, 1 (2004).
- ²¹P. Collins, *Dyn. Syst.* **20**, 369 (2005).
- ²²P. Collins, *Exp. Math.* **14**, 75 (2005).
- ²³R. W. Easton, *Transactions of the American Mathematical Society* **294**, 719 (1986).
- ²⁴R. W. Easton, (Oxford Univ. Press, 1998).
- ²⁵V. Rom-Kedar, *Physica D: Nonlinear Phenomena* **43**, 229 (1990).
- ²⁶V. Rom-Kedar, *Nonlinearity* **7**, 441 (1994).
- ²⁷B. Ruckerl and C. Jung, *Journal of Physics A: Mathematical and General* **27**, 55 (1994).
- ²⁸C. Lipp and C. Jung, *Journal of Physics A: Mathematical and General* **28**, 6887 (1995).
- ²⁹C. Jung and A. Emmanouilidou, *Chaos: An Interdisciplinary Journal of Nonlinear Science* (2005).
- ³⁰R. M. Frongillo, arXiv preprint arXiv:1001.4211 (2010).
- ³¹S. Day, R. Frongillo, and R. Trevino, *SIAM Journal on Applied Dynamical Systems* **7**, 1477 (2008).
- ³²R. Hagiwara and A. Shudo, *Journal of Physics A: Mathematical and General* **37**, 10521 (2004).
- ³³M. Hénon, *Communications in Mathematical Physics* **50**, 69 (1976).
- ³⁴Z. Arai, *Experimental Mathematics* **16**, 181 (2007).
- ³⁵P. S. Pachecho, *Parallel programming with MPI* (Morgan Kaufmann, 1997).
- ³⁶J. Nickolls, I. Buck, M. Garland, and K. Skadron, *Queue* **6**, 40 (2008).
- ³⁷K. A. Mitchell and J. B. Delos, *Physica D: Nonlinear Phenomena* **229**, 9 (2007).
- ³⁸T. Topçu and F. Robicheaux, *Journal of Physics B: Atomic, Molecular and Optical Physics* **40**, 1925 (2007).